JACS
JOURNAL OF THE AMERICAN CHEMICAL SOCIETY

Article

pubs.acs.org/JACS

Digenite Nanosheets Synthesized by Thermolysis of Layered Copper-Alkanethiolate Frameworks

Whitney Bryks, Eduardo Lupi, Charles Ngo, and Andrea R. Tao*

Department of NanoEngineering, University of California, San Diego, 9500 Gilman Drive MC 0448, La Jolla, California 92039-0448, United States

Supporting Information

ABSTRACT: Copper sulfide nanocrystals support localized surface plasmon resonances in the near-infrared wavelengths and have significant potential as active plasmonic nanomaterials due to the tunability of this optical response. While numerous strategies exist for synthesizing copper sulfide nanocrystals, few methods result in nanocrystals with both controlled morphological shapes and crystallinity. Here, we synthesize and characterize ultrathin (<5 nm) Cu_9S_5 nanosheets that are formed by solventless thermolysis, utilizing Cu alkanethiolates as single-source precursors. Layered Cu alkanethiolate precursors adopt a highly ordered structure which can be further stabilized in the presence of Cl^- and also serve to template the formation of nanosheets. We show that, in the absence of Cl^-, only isotropic and disk-like $Cu_{2-x}S$ nanocrystals form. These findings offer further insight into the use of layered metal−organic single-source precursors as templates for anisotropic nanocrystal growth.

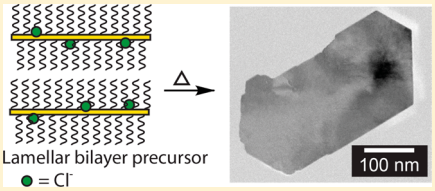

INTRODUCTION

Low-dimensional metal and semiconducting nanostructures that support localized surface plasmon resonances (LSPRs) are highly desired materials due to their ability to propagate, manipulate, and confine light. In particular, anisotropic nanostructures that possess well-defined edges and facets exhibit strong electromagnetic confinement effects that give rise to diverse optical phenomena.[1−3] Such plasmonic nanomaterials have impacted research in a broad range of applications where light localization or focusing is key, including platforms for optical spectroscopy, photovoltaics, and near-field microscopy.[4−7] LSPRs in the near-IR can be excited by fabricating highly anisotropic Ag or Au nanoparticles or by arranging metal nanoparticles into clusters.[8−10] For example, Au nanorods possess elongated shapes that enable LSPR excitation from 500 to over 1300 nm[11] and have been demonstrated as a viable contrast agent for photothermal therapy and photoacoustic imaging.[12−14] However, field localization in the near- to mid-IR range is limited by the intrinsic electromagnetic permittivity of Ag and Au.[15] Few metals are capable of supporting LSPRs in the IR range because they are highly absorbing and possess interband transitions at these wavelengths.[15] In addition, conventional metals used in plasmonic applications possess large free carrier densities ($>10^{22}$ cm^{-3}) that are not readily modulated by chemical or electrical means, impeding the ability to actively tune the dielectric response of the corresponding nanomaterials.

More recent focus has been extended to nanocrystals composed of highly doped semiconductor nanocrystals (SNCs) that exhibit LSPRs in the near- to mid-IR range, such as $Cu_{2-x}S$,[16−18] $Cu_{2-x}Se$,[19,20] highly doped ZnO,[21] and Sb-doped SnO_2.[22] These SNCs exhibit appropriate electromagnetic permittivities and sufficiently large free carrier concentrations to support LSPR excitations in the IR at frequency ranges far beyond what can be achieved by metallic nanostructures.[23,24] In addition, SNCs have demonstrated a high degree of LSPR tunability achieved through carrier density modulation, either by material doping (e.g., with In, Sn, Al) or by self-doping (e.g., introduction of holes via oxidative processes).[25−27,20] Because of their tunable IR response, SNCs could provide unprecedented opportunities for plasmonics in a new range of fields where manipulation or focusing of IR light is critical, including wireless telecommunication,[28] chemical sensing,[29,30] bioimaging,[31−34] and IR spectroscopy.[35−37]

For applications that depend on IR light focusing, a major challenge is the fabrication of highly anisotropic SNCs that support strong electromagnetic field localization. Of particular interest are two-dimensional (2D) nanomaterials, which display unique optoelectronic and mechanical properties resulting from in-plane confinement.[38−40] Such low-dimensional materials are often prepared by solvothermal routes. For instance, coordinating surfactant molecules can act in tandem with halide ions to promote planar growth and shape-focusing effects in CuS nanocrystals.[41] Another successful strategy for achieving shaped SNCs is by employing a molecular template, where low-dimensional nanocrystal morphologies are achieved using organic coordinating ligands to confine crystal growth. Such templates typically rely on the self-assembly of surfactant molecules into supramolecular structures such as micelles and bilayers that limit growth to just one or two dimensions. For example, CuS nanorods with subnanometer thickness were grown by sulfidation of $Cu[CH_3(CH_2)_{18}COO]_2$ precursors,

Received: August 8, 2016
Published: September 22, 2016

DOI: 10.1021/jacs.6b08264
J. Am. Chem. Soc. 2016, 138, 13717−13725

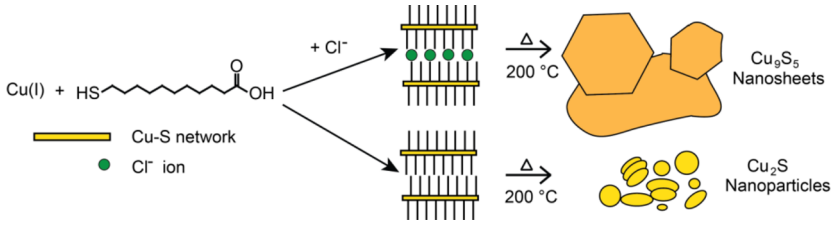

Figure 1. Reaction scheme for digenite sheets and chalcocite particles. Decomposition of $CuSC_{10}H_{20}COOH$ leads to oval or discotic chalcocite nanoparticles. Cl^- incorporation during supramolecular assembly leads to an alternative decomposition mechanism and nanosheet product.

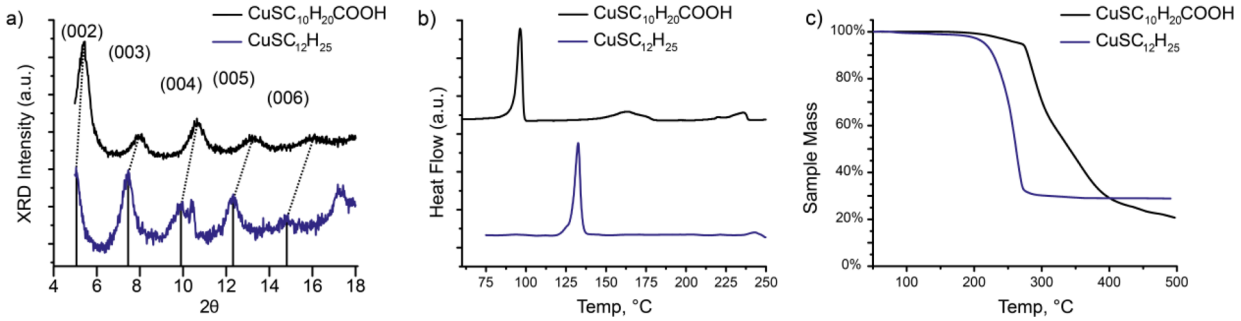

Figure 2. Comparison of $CuSC_{12}H_{25}$ and the bifunctionalized $CuSC_{10}H_{20}COOH$ precursor compounds. (a) XRD patterns for each precursor, demonstrating both have lamellar bilayer structures, while the DSC curves (b) and TGA curves (c) show show the change in thermal properties.

where $Cu[CH_3(CH_2)_{18}COO]_2$ forms a bilayer structure on a solid support. This bilayer serves as a template by confining Cu^{2+}, yielding arrays of ultrathin CuS nanorods upon sulfidation.[42] In a similar fashion, PbS quantum platelets were prepared using an alkylamine lamellar bilayer as a template. In this approach, *n*-octylamine formed lamellar mesophases *in situ*, leading to 2D nucleation and growth of PbS nanosheets from lead(II) acetate $[Pb(OAc)_2]$ and S^{2-} provided by thiourea.[43] In each of these examples, strong ligands (typically containing amine and carboxylate moieties) coordinate to metal ions while close-packed alkyl components provide confinement of SNC nucleation and growth processes.

Ag and Cu alkanethiolates are self-assembled supramolecular compounds that also form supramolecular structures, but are particularly notable because they take the form of liquid crystals with lamellar and micellar phases.[44−49] Previously, we and others demonstrated that $Cu_{2-x}S$ nanocrystals with disk-like shapes could be synthesized using Cu alkanethiolate precursors, which serve as both a shape-controlling template and a single-source precursor for SNC formation.[50,51] We were able to isolate intact supramolecular Cu alkanethiolates in both the layered and micellar forms, which we then used as templates for the formation of anisotropic SNC shapes such as nanosheets and nanodisks, respectively. One promising strategy to form higher aspect-ratio 2D SNCs utilized $CuSC_4H_9$ precursors, which maintain lamellar structures at thermolysis temperatures of ∼200 °C to form ultrathin (∼5 nm) $Cu_{2-x}S$ nanosheets.[51] However, we observed that the supramolecular structure of $CuSC_4H_9$ was significantly less stable than longer-chained Cu alkanethiolates, which we attributed to weaker in-plane van der Waals forces stabilizing the lamellar form. As a result, $CuSC_4H_9$ is more susceptible to disorder and the lamellar structure tends to degrade over time. This instability limited the size of resulting $Cu_{2-x}S$ nanosheets to widths of approximately 25 nm.

To obtain higher aspect-ratio 2D SNCs, it would be advantageous to develop single-source precursors that possess both a high degree of lamellar order and greater supramolecular stabilities at working thermolysis temperatures. Toward this end, we have explored the synthesis of single-source precursors that possess increased in-plane interactions to template the formation of $Cu_{2-x}S$ nanosheets. In this work, we report the synthesis and characterization of single-source Cu alkanethiolate precursors generated from bifunctional alkanethiols that are terminated with carboxylic acid groups. Increased in-plane interactions due to hydrogen bonding or attractive electrostatic interactions enable the preservation of lamellar supramolecular structures during thermolysis reactions. We also observe that bifunctional precursors enable the intercalation of halide ions, which further stabilizes the lamellar structure. Figure 1 shows the schematic for precursor formation with and without intercalated Cl^- and then subsequent precursor thermolysis to form copper sulfide. The stabilization of the lamellar bilayer structure with intercalated Cl^- leads to 2D nucleation and growth of Cu_9S_5 sheets rather than $Cu_{2-x}S$ particles. The data obtained allow us to posit a mechanism, and last, the resulting nanosheets are characterized by photoluminescence and absorption spectroscopy to determine their optical properties.

RESULTS AND DISCUSSION

$CuSC_{10}H_{20}COOH$ precursors were synthesized by precipitating Cu(OAc) with $HSC_{10}H_{20}COOH$ in solution (see experimental for more details). The isolated powder was analyzed with X-ray diffraction (XRD), differential scanning calorimetry (DSC) and thermal gravimetric analysis (TGA) to characterize molecular structure and thermal properties. Figure 2a shows the XRD spectrum for $CuSC_{10}H_{20}COOH$ and contrasts the results with Cu dodecanethiolate ($CuSC_{12}H_{25}$), which is made by similar precipitation methods.[51] The XRD spectra for both precursors possess sharp peaks that correspond to equally spaced lamellar bilayers, where the *d*-spacing between bilayers is calculated to be 3.25 nm for $CuSC_{10}H_{20}COOH$ and 3.45 nm for $CuSC_{12}H_{25}$. However, both thiol ligands in all-trans conformation are expected to be ∼1.5 nm in length, while the presence of the terminal −COOH

DOI: 10.1021/jacs.6b08264
J. Am. Chem. Soc. 2016, 138, 13717−13725

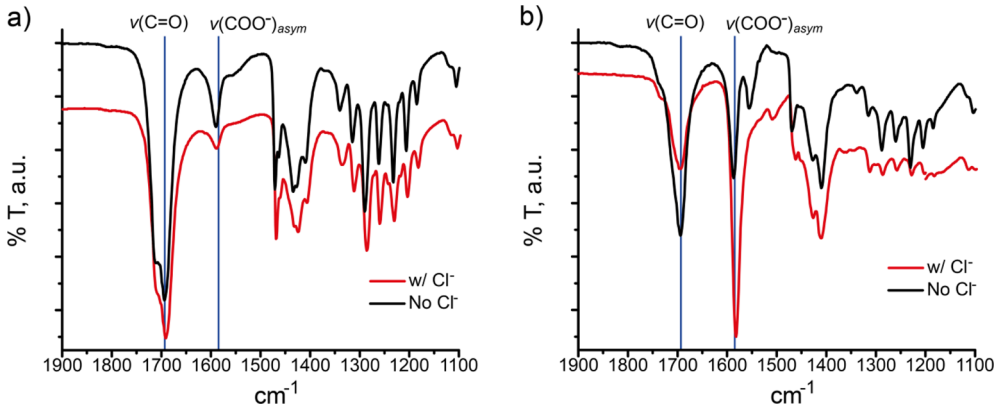

Figure 3. FTIR spectra of $CuSC_{10}H_{20}COOH$ precursor. Red line denotes Cl^- modified precursor (Cl = 20% Cu composition). (a) As-made precursors and (b) both precursors after thermal annealing at 200 °C for 10 min.

Table 1. FTIR Assignments of $CuSC_{10}H_{20}COOH$ Precursor Synthesized with and without Cl^-[a]

	sans Cl^-		with Cl^-	
assignment	preanneal	postanneal	preanneal	postanneal
$\nu(C{=}O)$	1694	1694	1694	1696
$\nu(COO^-)_{asym}$	1590	1587	1591	1584
$\delta(CH_2)$	1471	1470	1471	1464
$\delta(CH_2)$	1434	1427	1434	1429
$\nu(COO^-)_{sym}$	1409	1410	1408	1412
$\delta(CCH)$	1200−1300	1200−1300	1200−1300	1200−1300

[a]Each is shown pre- and post-annealing.

group in $CuSC_{10}H_{20}COOH$ results in a decrease in the interlayer *d*-spacing parameter by approximately 0.2 nm. We attribute this to strong hydrogen-bonding interactions between terminal −COOH groups, where some overlap of the carboxyl groups establishes a highly coordinated hydrogen-bonding network and slightly contracts the bilayer thickness.

Figure 2b shows DSC thermograms for $CuSC_{10}H_{20}COOH$ and $CuSC_{12}H_{25}$. Sharp endothermic peaks are indicative of structural transformations for $CuSC_{10}H_{20}COOH$ and $CuSC_{12}H_{25}$ at 94 and 132 °C, respectively. We previously identified that the peak for $CuSC_{12}H_{25}$ near 132 °C corresponds to a molecular rearrangement from a crystalline lamellar to a columnar mesophase, which is observed visually as a melting event from a tan-white powder to a viscous yellow fluid. For $CuSC_{10}H_{20}COOH$, the endothermic peak at 94 °C is more difficult to assign. When heated beyond 94 °C, the precursor powder loses granular texture and changes color, but remains solid. When heated between 150 and 175 °C, for which we observe a minor endothermic event on the DSC thermogram, the $CuSC_{10}H_{20}COOH$ precursor is observed to melt into a lower viscosity fluid. We believe the first transition at 94 °C corresponds to a smectic mesophase, while the higher-temperature phase transition corresponds to rearrangement into the columnar mesophase.

Figure 2c shows the TGA curves for $CuSC_{10}H_{20}COOH$ and $CuSC_{12}H_{25}$. The thermolysis byproducts (primarily dialkyl sulfides) show that the mass loss onset is ∼70 °C greater for $CuSC_{10}H_{20}COOH$ than for $CuSC_{12}H_{25}$. The higher evaporation temperature observed for $CuSC_{10}H_{20}COOH$ is attributed to intermolecular interactions between the polar −COOH groups. The TGA curve for $CuSC_{12}H_{25}$ shows a mass retention of approximately 30.0%, which correlates well with the formation of Cu_2S stoichiometry. In contrast, the curve for $CuSC_{10}H_{20}COOH$ shows continued mass loss up to 500 °C, dipping below the expected 28% mass retention for Cu_2S. This indicates that the $CuSC_{10}H_{20}COOH$ precursor is more stable and undergoes slower C−S thermolysis to the point where decomposition occurs in lieu of stoichiometric Cu_2S generation.

To understand how the intermolecular forces between these single-source precursors can be exploited for tuning thermal stability, we further explored how deprotonation of the −COOH group affects the mesophase transitions of the supramolecular $CuSC_{10}H_{20}COOH$ thermolysis precursor. In general, conversion of −COOH to $-COO^-$ is expected to create electrostatic repulsive forces that might serve to increase the separation distance between the individual lamella. To do so, we incorporated halide ions into the precursor by using Cu(I) halides as the Cu source. While halides incorporated poorly into $CuSC_{12}H_{25}$, they were readily incorporated into $CuSC_{10}H_{20}COOH$, and this was found to drastically alter the precursor's thermal characteristics. According to energy dispersive spectroscopy (EDS) analysis, the Cl^- intercalated is 48% as great as the Cu content by atomic weight, for the approximate formula $[CuSC_{10}H_{20}COOH]\cdot 1/2Cl$. To examine how Cl^- intercalation affects precursor thermolysis, we performed Fourier transform IR spectroscopy (FTIR) on both Cl^--intercalated and pristine samples of $CuSC_{10}H_{20}COOH$ upon thermal treatment. Figure 3 shows FTIR spectra obtained for each sample before and after thermal annealing of the precursors at 200 °C for 10 min. Figure 3a shows the as-made precursors, which both possess a strong $\nu(C{=}O)$ stretch near 1698 cm^{-1} and a weaker $\nu(COO^-)_{asym}$ mode at 1592 cm^{-1}. This indicates that prior to heating, both the pristine and Cl^--intercalated $CuSC_{10}H_{20}COOH$ are present as the carboxylic acid and not the deprotonated carboxylate. After thermal annealing, the precursors were cooled to room temperature.

DOI: 10.1021/jacs.6b08264
J. Am. Chem. Soc. 2016, 138, 13717−13725

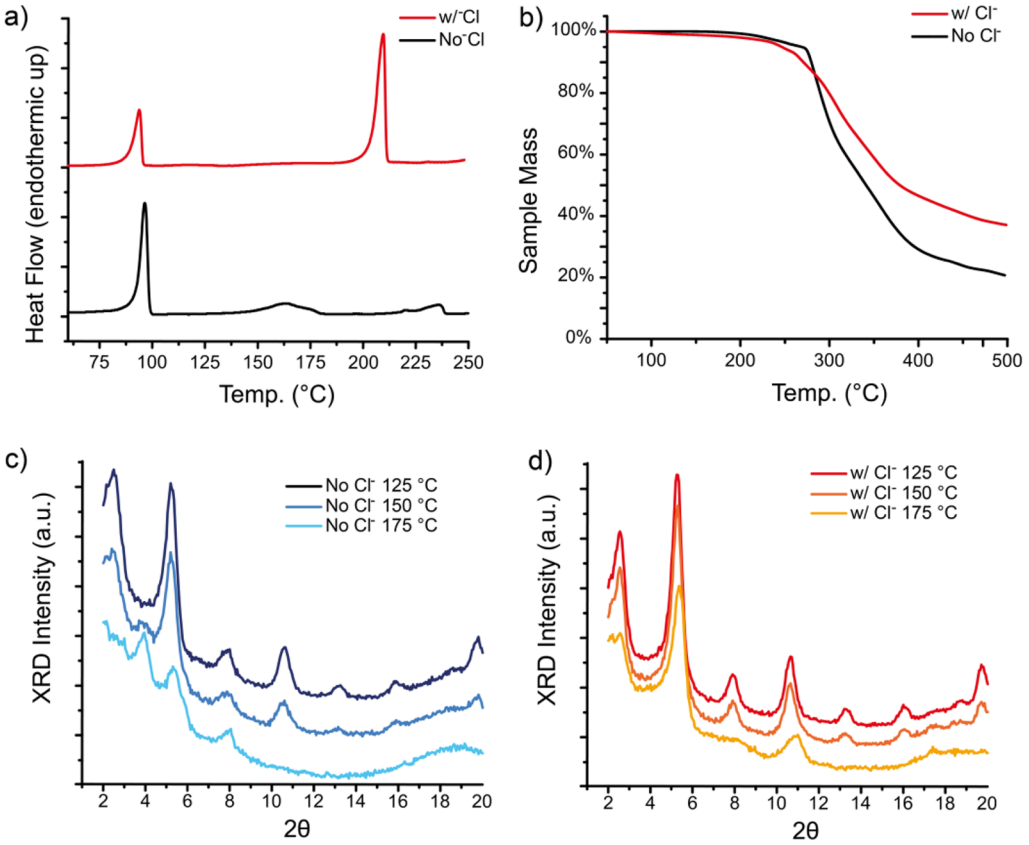

Figure 4. Thermal properties of pristine and Cl-intercalated $CuSC_{10}H_{20}COOH$ precursors as measured by (a) DSC and (b) TGA. (c,d) Characterization of the pristine and intercalated precursors by *in situ* high-temperature XRD, with spectra taken at 125, 150, and 175 °C for $CuSC_{10}H_{20}COOH$ prepared without and with Cl^- respectively.

The FTIR spectra in Figure 3b shows that conversion from carboxylic acid to carboxylate takes place for both the pristine and Cl^--intercalated $CuSC_{10}H_{20}COOH$. For the pristine precursor, annealing increases the $\nu(COO^-)_{asym}$ to $\nu(C{=}O)$ intensity ratio from 0.32 to 0.70, which is a 120% increase. For the Cl^--intercalated precursor, this conversion is significantly higher and the intensity ratio increases from 0.17 to 1.19, corresponding to a 590% increase. These FTIR assignments are provided in Table 1.

Figure 4 compares thermal properties of the pristine and Cl^--intercalated $CuSC_{10}H_{20}COOH$ precursors. DSC thermograms are shown in Figure 4a. The presence of Cl^- is not found to affect the endothermic transition at 94 °C, and both powders were observed to lose their granular textures and take on a viscous gel-like appearance. However, the presence of Cl^- suppresses the broad endothermic peak centered near 164 °C, and instead the Cl^--intercalated $CuSC_{10}H_{20}COOH$ shows an endothermic peak centered near 210 °C. Side-by-side visual observation during the heating of both compounds shows that, near the temperature of 175 °C, the pristine $CuSC_{10}H_{20}COOH$ exhibits a greater loss of viscosity. These data suggest that $CuSC_{10}H_{20}COOH$ undergoes a phase transition near 164 °C that is suppressed by the intercalation of Cl^-. Figure 4b shows TGA curves for the pristine and Cl^--intercalated $CuSC_{10}H_{20}COOH$ precursors heated at a rate of 5 °C min^{-1}. Intercalated Cl^- is observed to slow the rate of mass loss. This could be due to Cl^- coordination to Cu, which could weaken the Cu−S bond and by extension increase the energetic barrier for C−S bond thermolysis. TGA curves also show that Cl^--intercalated $CuSC_{10}H_{20}COOH$ retains a significantly greater mass at the final temperature of 500 °C. This is likely due to the incorporation of Cl^- in the decomposed product. EDX data shown in Table 2 present a positive correlation between precursor [Cl^-] and product [Cl^-], which is likely to occur if Cl^- is coordinating to Cu within the precursor.

Table 2. Lamellar Bilayer d-Spacing Shown As a Function of Cl^- Content

Cl (% of Cu)	48%	41%	27%	23%
d-spacing (nm)	3.342	3.337	3.300	3.274

To confirm whether the lamellar structure is retained at thermolysis temperatures, we carried out *in situ* XRD measurements of the pristine and Cl^--intercalated $CuSC_{10}H_{20}COOH$ precursors near the mesophase transitions observed by DSC. Figure 4c−d shows the XRD data for pristine and intercalated Cl^- samples heated at T = 125, 150, and 175 °C. At temperatures up to 125 °C, no significant features distinguish the two compounds, and the peaks representing a lamellar bilayer spacing of d = ∼3.3 nm are prominent near 2θ = 5.5°, 8°, and 10.5°. Between 150 and 175 °C, the pristine precursor shows a greater decrease in lamellar order, which can be seen as a decrease in the intensity and a broadening of the peaks at 2θ = 5.5° and 10.5°, with the latter disappearing altogether. This decrease in lamellar character is accompanied by the emergence of a new peak at 2θ = 4°, correlating to a spacing parameter of 2.24 nm. This is consistent with the *d*-spacing observed for columnar meso-

DOI: 10.1021/jacs.6b08264
J. Am. Chem. Soc. 2016, 138, 13717−13725

phases.[48,49] These thermal data strongly suggest that Cl^- serves to stabilize the lamellar phase.

In order to better understand the role that Cl^- plays in SNC nucleation and growth, we tuned $[Cl^-]$ across a range of Cl:Cu ratios. We achieved an indirect means of modulating Cl^- intercalation in the $CuSC_{10}H_{20}COOH$ precursor by varying the concentration of the solution it is precipitated from. Cl:Cu ratios were computed from energy dispersive spectroscopy (EDS) of the precursors (see experimental section for more details). The EDS results of this series are shown in Table 2. Expressed as a percentage of the Cu atomic weight %, the $[Cl^-]$ of this series was found to be approximately 23%, 27%, 41%, and 48%. We then carried out XRD analysis to determine where the intercalated Cl^- resides. Two different sites for Cl^- are possible: (i) coordinated to Cu near the Cu−S network, or (ii) near the highly polar carboxyl groups in the center of the bilayer. The presence of Cl^- in position (i) should show no change in XRD data; however Cl^- in position (ii) should expand the lamellar bilayer spacing. Figure 5 shows the XRD

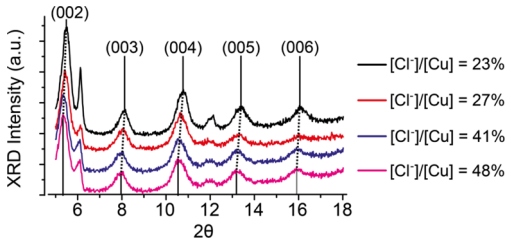

Figure 5. XRD of $CuSC_{10}H_{20}COOH$ precursors prepared with varying $[Cl^-]$. The interlayer *d*-spacing is found to increase with $[Cl^-]$.

patterns for samples prepared with varying $[Cl^-]$. Whereas $CuSC_{10}H_{20}COOH$ synthesized from Cu(OAc) has a lamellar bilayer spacing parameter of 3.25 nm, $CuSC_{10}H_{20}COOH$ synthesized from CuCl with $[Cl^-]/[Cu]$ = 48% showed a lamellar bilayer spacing of 3.34 nm, or a 0.9 Å increase. The lamellar bilayer expansion suggests that intercalated Cl^- ions reside between carboxyl groups. This placement makes sense in terms of sterics; the alkyl groups in self-assembled metal alkanethiolates are thought to be similar to an alkanethiol self-assembled monolayer, where densely packed alkanes should not be sterically accommodating for Cl^-. It should be noted that an additional set of XRD peaks is present at 2θ = 6° and 12°. These peaks are often present in the precursor at room temperature, which we attribute to a bilayer stacking defect. Interestingly, the peaks are no longer present when the precursor is heated to temperatures exceeding 125 °C (Figure 4c,d), which suggests that the stacking defect is annealed when the precursor undergoes the lower-temperature phase transition at 94 °C.

Figure 6 shows the SNCs obtained as products for $CuSC_{10}H_{20}COOH$ precursors with varying $[Cl^-]$ contents after carrying out thermolysis at 200 °C for 6 h. XRD and transmission electron microscopy (TEM) imaging of the products show that higher $[Cl^-]$ favors the formation of digenite (Cu_9S_5) SNCs with a 2D nanosheet morphology, while lower $[Cl^-]$ favors *β*-chalcocite (Cu_2S) SNCs with disk-like morphology. Figure 6a shows the XRD patterns from lowest (top) to highest $[Cl^-]$ contents (bottom). The sample with the lowest $[Cl^-]$ content produced *β*-chalcocite SNCs, similar to products obtained for thermolysis of pristine $CuSC_{10}H_{20}COOH$. However, when $[Cl^-]$ increases beyond

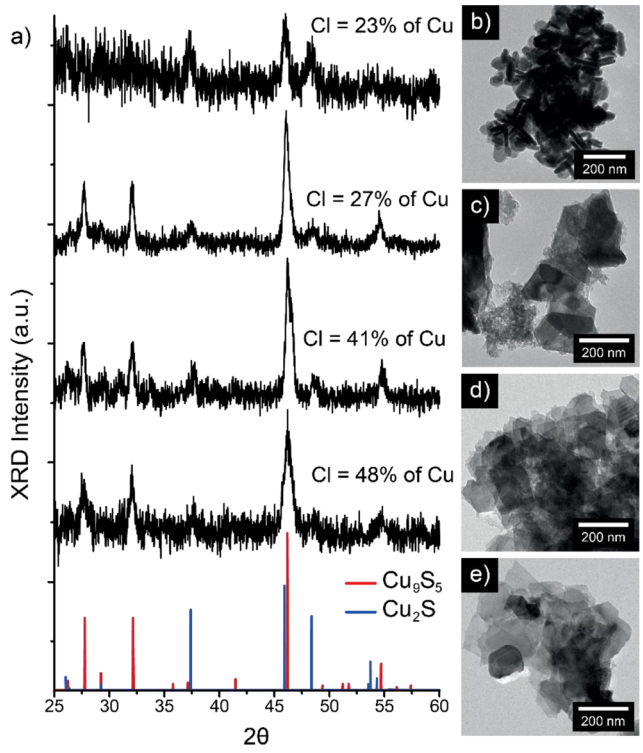

Figure 6. Effect of varying Cl^- incorporation. (a) XRD patterns of nanoparticles obtained from thermolysis of precursor containing various $[Cl^-]$, showing that chalcocite phase preferred sans chloride gives rise to digenite when chloride content increases. (b−e) TEM images for the respective XRD patterns, from least to most $[Cl^-]$.

25%, the crystal phase of the SNC product is observed to be predominantly digenite (Cu_9S_5). Figure 6b-e shows the corresponding TEM images with increasing Cl^- intercalation. For the precursor with $[Cl^-]$ = 23% (Figure 6b), disk-like SNCs are the majority product and sheets are rarely observed. With $[Cl^-]$ = 27% of Cu content in the precursor (Figure 6c), disk-like particles are no longer observed and more distinct 2D morphologies are present. However, much of the material is observed to exist within large, nondispersible aggregates. With $[Cl^-]$ = 41%−48% of Cu content in the precursor (Figure 6d,e), 2D SNCs are observed as the majority product.

Table 3 shows EDS of the SNC products shown in Figure 6b-e. The data demonstrated an obvious trend between $[Cl^-]$

Table 3. EDX results comparing $[Cl^-]$ of the precursor vs. that of the product after thermolysis for 6 h at 200 °C

Cl^- (% of Cu)				
Precursor	23%	27%	41%	48%
Product	8%	11%	16%	43%

in the precursor and $[Cl^-]$ in the thermolysis product. The amount of Cl^- intercalated within the product structure is substantial, reaching a ratio 2:5 with Cu. Because the increasing Cl^- content coincides with decreasing S content (Figure S1), this indicates that Cl^- is indeed intercalated and not simply present as surface species. The results suggest Cl^- is responsible for both the digenite phase and the nanosheet morphology of the SNCs obtained via thermolysis.

We further characterized the SNC products obtained after thermolysis at 200 °C for times of 30, 180, and 360 min. Figure

DOI: 10.1021/jacs.6b08264
J. Am. Chem. Soc. 2016, 138, 13717−13725

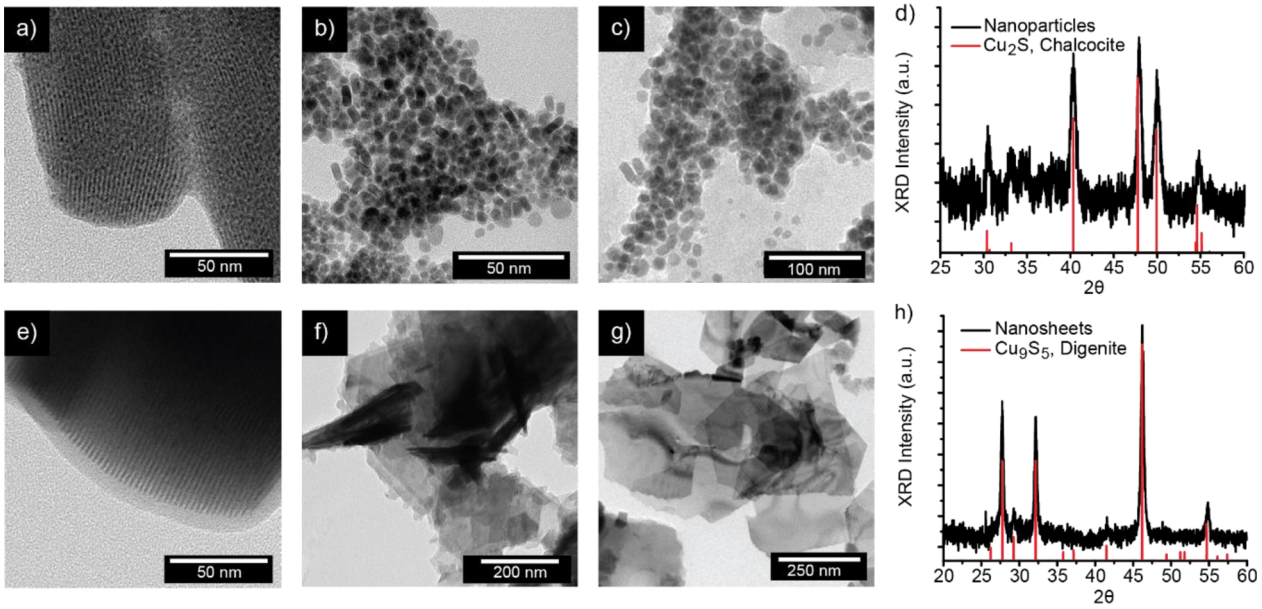

Figure 7. Time-dependent electron microscopy of chalcocite particle formation and digenite sheet formation. Top: compound (I) sans chloride after decomposition for (a) 30 min, (b) 180 min, (c) 360 min, and (d) the XRD pattern of the 360 min product corresponding to Cu_2S. Bottom: compound (I) with chloride after decomposition for (e) 30 min, (f) 180 min, (g) 360 min, and (h) the XRD pattern of the 360 min product corresponding to Cu_9S_5.

7a-c shows TEM images of the formation of β-chalcocite Cu_2S nanocrystals obtained with pristine $CuSC_{10}H_{20}COOH$. Small seed particles around 2 nm large are seen to precipitate within aligned columns of precursor material in the early stages of the reaction (Figure 7a). We previously observed aligned nanoparticle columns embedded in organic matrix during partial thermolysis of $CuSC_{12}H_{25}$. We attributed this alignment to the presence of the columnar mesophase during thermolysis of $CuSC_{12}H_{25}$. Mesogenic rearrangement to a columnar phase would explain the striated texture observed when $CuSC_{10}H_{20}COOH$ sans Cl^- is incompletely decomposed (Figure 7a). Image analysis of the striations in Figure 7a reveals a center-to-center spacing of ~2.3 nm. This spacing parameter correlates to the XRD peak at $2\theta = 4°$ observed at elevated temperature (Figure 4c). Figure 7b,c show that, with increased thermolysis time, larger particles are obtained with roughly discotic or ovoid morphology (diameter: 14.5 ± 3.8 nm; thickness: 9.6 ± 1.7 nm). The XRD pattern in Figure 7d matches β-chalcocite Cu_2S. This is consistent with our previous thermolyses of long-chained Cu-alkanethiolates, for which we obtained β-chalcocite nanodisks.

Figure 7e–g show time-dependent TEM imaging of $CuSC_{10}H_{20}COOH$ precursor generated from CuCl. In the presence of Cl^- an alternate SNC growth pathway is observed where nucleation and growth occurs in distinct 2D planes. In Figure 7e which shows TEM images of the SNC products after 30 min of thermolysis, aligned arrays of electron-dense material (which we attribute to the solid-state SNC product) appear embedded within low-contrast material. We attribute the low-contrast material to partially decomposed precursor. Figure 7f shows that, after 180 min, 2D sheets are obtained and many of these are unencapsulated. However, multiple sheets are observed to form large aggregates due to incomplete decomposition of the organic phase. Figure 7g shows that, after 6 h of thermolysis, free-standing nanosheets are obtained. The XRD pattern in Figure 7h best matches the metastable, rhombohedral form of digenite Cu_9S_5.

Mechanism for SNC Growth. To explain nanosheet formation we propose a mechanism where intercalated Cl^- stabilizes the lamellar phase during thermolysis. The thermal data demonstrates that Cl^- affects structure and C–S thermolysis of $CuSC_{10}H_{20}COOH$ precursor. DSC data does show a commonality between Cl^--bearing and Cl^--deficient precursor in the presence of an endothermic peak near 94 °C. The most feasible explanation here is that this peak corresponds to a crystalline lamellar to lamellar smectic transition, where minor alkyl chain disorder is present and adjacent lamella are capable of slipping. The transition to a lamellar smectic mesophase could enable reordering of lamellar domains and therefore explain why peaks observed at $2\theta = 6$ and 12° attributed to a stacking defect (Figure 5) are no longer present beyond 125 °C (Figure S4 and Figure 4c,d). This phase would further explain why the precursor is visually observed to change color and texture beyond 94 °C even as the high temperature XRD patterns show the structure is still lamellar. The DSC peak at 164 °C is likely the columnar mesophase transition and correlates with loss of lamellar character and emergence of a peak characteristic of the columnar phase as shown by XRD (Figure 4a,c). Conversely in the presence of Cl^-, the 164 °C DSC peak is suppressed, and heated precursor shows stronger retention of lamellar character (Figure 4b,d).

The exact role played by Cl^- is more difficult to decipher; although it should be present within the alkyl bilayer, the impact of Cl^- on thermolysis as shown by mass loss (Figure 4a) and retention of Cl^- within the crystallized product (Table 3) support that Cl^- coordinates to Cu during thermolysis and is subsequently incorporated into the crystal structure. A possible explanation is that conversion of $-COOH$ to $-COO^-$ (Figure 3) creates negative charges which help drive Cl^- from the alkyl bilayer toward Cu sites in the Cu–S plane. For Cl^- to stabilize the lamellar phase, it must either decrease the thermal disorder occurring among alkyl components or reinforce in-plane attractive forces. We find the latter explanation more compelling: Cl^- coordination to Cu within the Cu–S planes

DOI: 10.1021/jacs.6b08264
J. Am. Chem. Soc. 2016, 138, 13717–13725

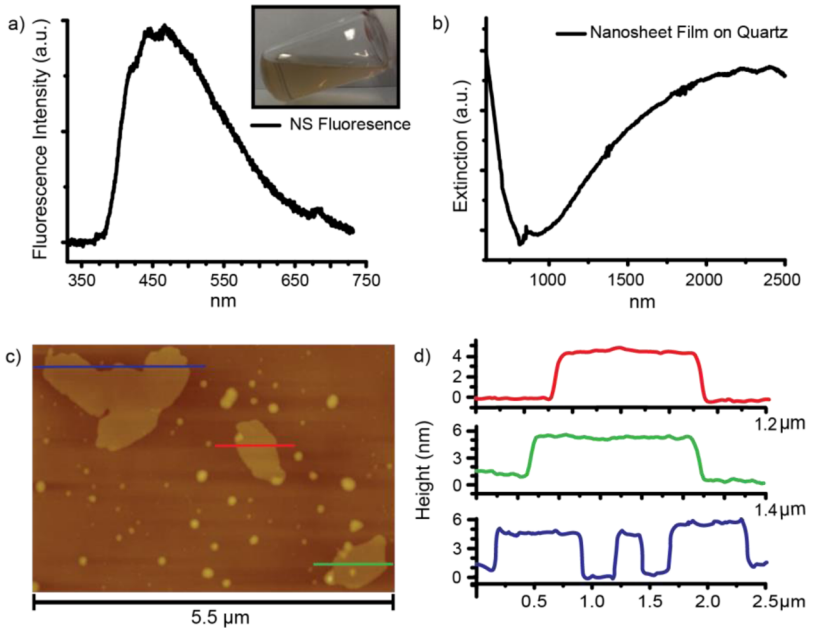

Figure 8. AFM and optical characterization of digenite nanosheets. (a) Photoluminescence spectrum of the digenite sheets dispersed in ethanol (inset: image of dispersion) using excitation of 325 nm. (b) Extinction spectrum of a film of digenite sheets made on a transparent quarts substrate, with an LSPR peak near 2400 nm attributed to the out of plane mode. (c) AFM topology image showing where height profiles were taken along 3 of the digenite nanosheets. (d) Height profiles are plotted which demonstrate a high degree of planarity and a thickness of 4.0−4.5 nm.

represents another interaction which must be overcome prior to mesogenic rearrangement. During thermolysis, this lamellar template serves to encourage anisotropic nucleation and growth along the Cu−S planes, resulting in nanosheet formation. The formation of digenite phase $Cu_{1.8}S$ has previously been shown to result when CuCl is used as the copper source and can also be explained by intercalated Cl^-.[52,53]

Work conducted by van der Stam et al. previously demonstrated a similar system where $Cu_{2-x}S$ nanosheets were obtained from a solvothermal reaction in 1-octadecene/TOPO which generated a halide-stabilized Cu alkanethiolate intermediate.[54] The authors suggested that the nanosheet template is offered by the columnar mesophase of the Cu alkanethiolate existing in solution at elevated temperature. Our data support the conclusion by van der Stam et al. that halides coordinate directly to Cu to influence thermolysis, which manifests as substantial Cl^- content in the crystallized product (Figure S1). However, our results suggest that halide interactions stabilize the lamellar phase during thermolysis leading to nanosheet formation and that columnar rearrangement leads to the formation of small nanoparticles (Figure S2). The XRD patterns of Cl^- stabilized precursor at 175 °C in Figure 4c indicate a layered structure with no evidence of columnar rearrangement. Furthermore, decomposition of this precursor at 175 and 180 °C produces nanosheets, although at these temperatures they are often still adjoined by precursor material (Figure S2). The data, taken together, support conclusions from our previous work that mesogenic rearrangement of Cu alkanethiolates during thermolysis causes the formation of disk-like nanocrystals, while nanosheets are realized from thermolysis in the lamellar phase.[51]

Optical Characterization and AFM of SNC Nanosheets. Figure 8 shows photoluminescence (PL) spectroscopy and visible to near-infrared (vis/NIR) absorption spectroscopy, as well as atomic force microscopy (AFM), of the nanosheets obtained from decomposition of the Cl^- intercalated precursor. The PL emission spectra shown in Figure 7a ($\lambda_{excitation}$ = 325 nm) were obtained in an ethanol dispersion and shows the PL emission band centered around 450 nm. This is in contrast to previously reported Cu_9S_5 nanoparticles where emission was centered between 387 and 440 nm depending on the excitation wavelength.[55] Curiously, in this report CuS particles showed identical PL emission to the Cu_9S_5 particles. Emission of Cu_9S_5 nanocrystals with irregular octahedral shape centered at 360 nm using $\lambda_{excitation}$ = 300 nm has also been reported.[56] Interestingly, this report again showed invariance between the crystal phase and PL emission; particle compositions which included CuS, Cu_9S_5, and a CuS-Cu_7S_4 mixture all produced PL emission at 360 nm. While we might expect the ultrathin nature of our Cu_9S_5 sheets to increase photoemission energy due quantum confinement, this was not observed, and so we note that photoemission in the $Cu_{2-x}S$ system is still not well-understood.

UV−vis−NIR absorption spectra were taken with a dried dispersion of nanosheets on a quartz substrate. Copper sulfides are known to support LSPR bands in the NIR due to the high mobility and density of holes as free charge carriers. The LSPR of the Cu_9S_5 nanosheets in Figure 8b is centered around 2400 nm and observed to be quite broad. Based on our previous characterization of $Cu_{2-x}S$ nanodisks,[18] we assign this LSPR band to the resonant out-of-plane mode. The in-plane mode expected for a 2D structure is predicted to appear at lower energy and due to a large degree of noise on our spectrophotometer, our measurement was limited to 2500 nm. The breadth of the out-of-plane mode may arise from stacked nanosheets resulting in plasmonic coupling, which would serve to red-shift and broaden the mode.

Figure 8c shows the AFM topology of several large sheets, with height profiles consistently between 4.0 and 4.5 nm (Figure 8d). Although several faceted edges are observed, the nanosheet sizes and edge morphologies are not uniform, consistent with TEM images. AFM analysis of multiple SNC

DOI: 10.1021/jacs.6b08264
J. Am. Chem. Soc. 2016, 138, 13717−13725

samples indicates that nanosheets possess a uniform thickness of 4−4.5 nm (Figure S3). Many rounded spots observed in the AFM scans are attributed to incompletely decomposed precursor material, which is difficult to separate via centrifugation because the precursor is insoluble in solvents at room temperature. The largest nanosheet (blue section) in Figure 8a displays an edge length of 2.25 μm and a thickness of ∼4.5 nm for a total aspect-ratio of ∼500. To the best of our knowledge, this is the highest reported aspect ratio for a single freestanding copper sulfide nanosheet (of any phase) as verified by AFM.

CONCLUSIONS

The 2D metal-chalcogen networks formed via assembly of metal alkanethiolates provide a viable platform for 2D nanocrystal synthesis. In our previous work, we showed that the length of the alkyl thiol chain used dictates the precursor's structural phase during thermolysis. Here, we showed that the lamellar phase is stabilized at the thermolysis temperature by using a combination of in-plane H-bonding provided by terminal carboxyl groups and the addition of intercalated Cl^- ions. Thermolysis of $[CuSC_{10}H_{20}COOH]\cdot 1/2Cl$ led to formation of ultrathin Cu_9S_5 nanosheets. This method presents the chemical design of a single source precursor which doubles as a morphological template. This mechanism may not be unique to Cu-based alkanethiolates, but may well carry over to other metals, and even other alkyl chalcogenols. This could potentially allow one to program metal chalcogenide composition and morphology all through rational design of the single source precursor. We are currently investigating the use of this templating motif as a general platform for the realization of metal chalcogenides with ultrathin 2D morphologies.

MATERIALS AND METHODS

Chemicals. All reagents were used as-purchased. 1-Dodecanethiol (98%), 11-mercaptoundecanol (97%), 11-mercaptoundecanoic acid (95%), and copper(I) acetate (97%) were purchased from Sigma-Aldrich. Copper(I) chloride was purchased from Fisher Scientific. Ethanol was purchased from Gold Shield Chemical Company. Chloroform was purchased from Avantor Performance Materials. Water was obtained via a Millipore Milli-Q Advantage A10 water filtration system. All reagents were used as purchased.

Preparation of $CuSC_{10}COOH$. The following synthesis for $CuSC_{10}COOH$ is representative of a standard reaction for producing $CuSC_{10}COOH$ without chloride. 11-Mercaptoundecanoic acid is (1.37 mmol) is dissolved in 1.37 mL of ethanol to make a 1 M solution. In a separate flask equipped with a stir bar, copper(I) acetate (0.687 mmol) is dispersed in 2.748 mL of water to make a 0.25 M dispersion which is stirred rapidly.

Copper(I) salts are generally insoluble; however, copper(II) is readily reduced to copper(I) by alkanethiols generating disulfide in the process, which was deemed undesirable here.

The ethanolic thiol solution is added dropwise to the copper solution while stirring, and a white slurry indicating the precipitation of $CuSC_{10}COOH$ is immediately observable. This is allowed to stir for 15 additional minutes. A milky white precipitate is obtained and isolated via centrifugation at 3000 rpms for 5 min. After the supernatant was decanted, the precipitate is washed with a 1:1 mixture of water and ethanol and centrifuged again under the same conditions. This process is repeated twice more; however, the last wash is performed with only ethanol and no water. The precipitate is then stored in a vacuum desiccator until dry of ethanol.

In order to prepare $CuSC_{10}COOH$ with chloride, copper(I) chloride is substituted in place of copper(I) acetate.

Synthesis of Chalcocite-Phase Nanoparticles. A 25 mg amount of the $CuSC_{10}COOH$ precursor generated from copper(I) acetate is measured into a scintillation vial under ambient conditions, capped tightly, and immersed in a hot oil bath at 200 °C for 6 h. The whitish powder melts into a viscous yellow fluid before gradually darkening to black with further decomposition. After the reaction is complete, the vial is cooled to room temperature. The black residue is dispersed in 12 mL of pure ethanol, through ample ultrasonication before being centrifuged down at 7,500 rpms for 7.5 min. After the supernatant was decanted, the particles are redispersed in ethanol, and this process is repeated 3 times. The final product is allowed to dry in a vacuum desiccator overnight to obtain a black powder.

Synthesis of Digenite Phase Nanosheets. To prepare digenite phase nanosheets, the preceding synthesis is used. However, 25 mg of $CuSC_{10}COOH$ precursor generated from Cu(I) chloride is used. Similarly, this powder is observed to change colors, from off-white to yellow-green and then black, and is accompanied by a change of texture indicative of melting albeit not into a fluid that can flow.

Sample Characterization. Powder X-ray diffraction (XRD) was performed using a Rigaku RU200B diffractometer running MDI Datascan5 software. The operating voltage was set to 100 kV with a step size of 0.02° and a dwell time of 1.0 s. Transmission electron micrsocopy (TEM) was performed on an FEI Tecnai G2 Sphera running a LaB_6 filament at 200 kV. A Gatan Ultrascan 1000 UHS CCD camera running Gatan Digital Micrograph was used for imaging. TEM samples were typically prepared by dispersing particles in ethanol and dropcasting directly onto a 200 mesh carbon-film Cu grid. Atomic force microscopy (AFM) was obtained using tapping mode on an Innova AFM, a Bruker controller, and the Nanodrive software. AFM samples were dropcast directly onto Piranha-washed Si chips. Thermogravimetric analysis (TGA) was performed using a PerkinElmer TGA 7 Thermogravimetric Analyzer attached to a PerkinElmer TAC 7/DX Thermal Analysis Controller. Optical absorption measurements were taken using a PerkinElmer Lambda-1050 spectrophotometer. Nanosheet samples were dropcast onto a quartz substrate for optical extinction spectra. Differential Scanning Calorimetry (DSC) was performed using a PerkinElmer PYRIS Diamond DSC. Fourier-Transform Infrared Spectroscopy (FTIR) was performed using a PerkinElmer UATR Two FT-IR Spectrometer running PerkinElmer Spectrum software. Energy dispersive spectroscopy (EDX) was obtained using a Philips XL30 ESEM with an Oxford EDX attachment. Cu foil was used for calibration prior to taking spectra, which were averaged over 3 spots per sample at 90 s acquisition per spot. Reported percentages of Cl represent Cl as a fraction of the Cu content.

ASSOCIATED CONTENT

Supporting Information

The Supporting Information is available free of charge on the ACS Publications website at DOI: 10.1021/jacs.6b08264.

EDX of nanosheet products, additional TEM imaging of nanosheet and nanoparticle growth, and additional nanosheet AFM (PDF)

AUTHOR INFORMATION

Corresponding Author

*atao@ucsd.edu

Notes

The authors declare no competing financial interest.

ACKNOWLEDGMENTS

This work was partly supported by the National Science Foundation, Grant No. CHE 150855.

DOI: 10.1021/jacs.6b08264
J. Am. Chem. Soc. 2016, 138, 13717−13725

REFERENCES

(1) Kottmann, J. P.; Martin, O. J. F.; Smith, D. R.; Schultz, S. *J. Microsc.* **2001**, *202* (1), 60−65.
(2) Papavassiliou, G. C. *Prog. Solid State Chem.* **1979**, *12* (3), 185−271.
(3) Xia, Y.; Halas, N. J. *MRS Bull.* **2005**, *30* (05), 338−348.
(4) Brolo, A. G.; Gordon, R.; Leathem, B.; Kavanagh, K. L. *Langmuir* **2004**, *20* (12), 4813−4815.
(5) Cubukcu, E.; Kort, E. A.; Crozier, K. B.; Capasso, F. *Appl. Phys. Lett.* **2006**, *89* (9), 093120−3.
(6) Haes, A. J.; Van Duyne, R. P. *J. Am. Chem. Soc.* **2002**, *124* (35), 10596−10604.
(7) Atwater, H. A.; Polman, A. *Nat. Mater.* **2010**, *9* (3), 205−213.
(8) Skrabalak, S. E.; Chen, J.; Sun, Y.; Lu, X.; Au, L.; Cobley, C. M.; Xia, Y. *Acc. Chem. Res.* **2008**, *41* (12), 1587−1595.
(9) Jensen, T. R.; Malinsky, M. D.; Haynes, C. L.; Van Duyne, R. P. *J. Phys. Chem. B* **2000**, *104* (45), 10549−10556.
(10) Gao, B.; Arya, G.; Tao, A. R. *Nat. Nanotechnol.* **2012**, *7* (7), 433−437.
(11) van der Zande, B. M. I.; Böhmer, M. R.; Fokkink, L. G. J.; Schönenberger, C. *J. Phys. Chem. B* **1997**, *101* (6), 852−854.
(12) Zhang, L.; Xia, K.; Lu, Z.; Li, G.; Chen, J.; Deng, Y.; Li, S.; Zhou, F.; He, N. *Chem. Mater.* **2014**, *26* (5), 1794−1798.
(13) Huang, X.; El-Sayed, I. H.; Qian, W.; El-Sayed, M. A. *J. Am. Chem. Soc.* **2006**, *128* (6), 2115−2120.
(14) Moon, H.; Kumar, D.; Kim, H.; Sim, C.; Chang, J. H.; Kim, J. M.; Kim, H.; Lim, D. K. *ACS Nano* **2015**, *9* (3), 2711−2719.
(15) Langhammer, C.; Kasemo, B.; Zoric, I. *J. Chem. Phys.* **2007**, *126* (19), 194702−11.
(16) Hsu, S.-W.; On, K.; Tao, A. R. *J. Am. Chem. Soc.* **2011**, *133*, 19072.
(17) Hsu, S.-W.; Bryks, W.; Tao, A. R. *Chem. Mater.* **2012**, *24* (19), 3765−3771.
(18) Hsu, S.-W.; Ngo, C.; Tao, A. R. *Nano Lett.* **2014**, *14* (5), 2372−2380.
(19) Dorfs, D.; Härtling, T.; Miszta, K.; Bigall, N. C.; Kim, M. R.; Genovese, A.; Falqui, A.; Povia, M.; Manna, L. *J. Am. Chem. Soc.* **2011**, *133* (29), 11175−11180.
(20) Kriegel, I.; Jiang, C.; Rodríguez-Fernández, J.; Schaller, R. D.; Talapin, D. V.; da Como, E.; Feldmann, J. *J. Am. Chem. Soc.* **2012**, *134* (3), 1583−1590.
(21) Kim, H.; Osofsky, M.; Prokes, S. M.; Glembocki, O. J.; Pique, A. *Appl. Phys. Lett.* **2013**, *102*, 171103.
(22) Zum Felde, U.; Haase, M.; Weller, H. *J. Phys. Chem. B* **2000**, *104* (40), 9388−9395.
(23) Luther, J. M.; Jain, P. K.; Ewers, T.; Alivisatos, A. P. *Nat. Mater.* **2011**, *10* (5), 361−366.
(24) Zhao, Y.; Pan, H.; Lou, Y.; Qiu, X.; Zhu, J.; Burda, C. *J. Am. Chem. Soc.* **2009**, *131* (12), 4253−4261.
(25) Niezgoda, J. S.; Harrison, M. A.; McBride, J. R.; Rosenthal, S. J. *Chem. Mater.* **2012**, *24* (16), 3294−3298.
(26) Wang, X.; Liu, X.; Yin, D.; Ke, Y.; Swihart, M. T. *Chem. Mater.* **2015**, *27* (9), 3378−3388.
(27) Greenberg, B. L.; Ganguly, S.; Held, J. T.; Kramer, N. J.; Mkhoyan, K. A.; Aydil, E. S.; Kortshagen, U. R. *Nano Lett.* **2015**, *15* (12), 8162−8169.
(28) Kahn, J. M.; Barry, J. R. *Proc. IEEE* **1997**, *85* (2), 265−298.
(29) Ogawa, S.; Okada, K.; Fukushima, N.; Kimata, M. *Appl. Phys. Lett.* **2012**, *100*, 021111.
(30) Stewart, M. E.; Anderton, C. R.; Thompson, L. B.; Maria, J.; Gray, S. K.; Rogers, J. A.; Nuzzo, R. G. *Chem. Rev.* **2008**, *108* (2), 494−521.
(31) Zhou, M.; Li, J.; Liang, S.; Sood, A. K.; Liang, D.; Li, C. *ACS Nano* **2015**, *9* (7), 7085−7096.
(32) Ku, G.; Zhou, M.; Song, S.; Huang, Q.; Hazle, J.; Li, C. *ACS Nano* **2012**, *6* (8), 7489−7496.
(33) Zhou, M.; Zhang, R.; Huang, M.; Lu, W.; Song, S.; Melancon, M. P.; Tian, M.; Liang, D.; Li, C. *J. Am. Chem. Soc.* **2010**, *132* (43), 15351−15358.
(34) Chen, F.; Hong, H.; Goel, S.; Graves, S. A.; Orbay, H.; Ehlerding, E. B.; Shi, S.; Theuer, C. P.; Nickles, R. J.; Cai, W. *ACS Nano* **2015**, *9* (4), 3926−3934.
(35) Ikehata, A.; Itoh, T.; Ozaki, Y. *Anal. Chem.* **2004**, *76* (21), 6461−6469.
(36) Baldassarre, L.; Sakat, E.; Frigerio, J.; Samarelli, A.; Gallacher, K.; Calandrini, E.; Isella, G.; Paul, D. J.; Ortolani, M.; Biagioni, P. *Nano Lett.* **2015**, *15* (11), 7225−7231.
(37) Chen, K.; Adato, R.; Altug, H. *ACS Nano* **2012**, *6* (9), 7998−8006.
(38) Wang, Q. H.; Kalantar-Zadeh, K.; Kis, A.; Coleman, J. N.; Strano, M. S. *Nat. Nanotechnol.* **2012**, *7* (11), 699−712.
(39) Chhowalla, M.; Shin, H. S.; Eda, G.; Li, L.-J.; Loh, K. P.; Zhang, H. *Nat. Chem.* **2013**, *5* (4), 263−275.
(40) Butler, S. Z.; Hollen, S. M.; Cao, L.; Cui, Y.; Gupta, J. A.; Gutiérrez, H. R.; Heinz, T. F.; Hong, S. S.; Huang, J.; Ismach, A. F.; Johnston-Halperin, E.; Kuno, M.; Plashnitsa, V. V.; Robinson, R. D.; Ruoff, R. S.; Salahuddin, S.; Shan, J.; Shi, L.; Spencer, M. G.; Terrones, M.; Windl, W.; Goldberger, J. E. *ACS Nano* **2013**, *7* (4), 2898−2926.
(41) Hsu, S.-W.; Ngo, C.; Bryks, W.; Tao, A. R. *Chem. Mater.* **2015**, *27* (14), 4957−4963.
(42) Mao, G.; Dong, W.; Kurth, D. G.; Möhwald, H. *Nano Lett.* **2004**, *4* (2), 249−252.
(43) Morrison, P. J.; Loomis, R. A.; Buhro, W. E. *Chem. Mater.* **2014**, *26* (17), 5012−5019.
(44) Dance, I. G.; Fisher, K. J.; Banda, R. M. H.; Scudder, M. L. *Inorg. Chem.* **1991**, *30* (2), 183−187.
(45) Baena, M. J.; Espinet, P.; Lequerica, M. C.; Levelut, A. M. *J. Am. Chem. Soc.* **1992**, *114* (11), 4182−4185.
(46) Bardeau, J. F.; Parikh, A. N.; Beers, J. D.; Swanson, B. I. *J. Phys. Chem. B* **2000**, *104* (3), 627−635.
(47) Sandhyarani, N.; Pradeep, T. *J. Mater. Chem.* **2001**, *11* (4), 1294−1299.
(48) Espinet, P.; Lequerica, M. C.; Martin-Alvarez, J. M. *Chem. - Eur. J.* **1999**, *5* (7), 1982−1986.
(49) Levchenko, A. A.; Yee, C. K.; Parikh, A. N.; Navrotsky, A. *Chem. Mater.* **2005**, *17* (22), 5428−5438.
(50) Sigman, M. B.; Ghezelbash, A.; Hanrath, T.; Saunders, A. E.; Lee, F.; Korgel, B. A. *J. Am. Chem. Soc.* **2003**, *125* (51), 16050−16057.
(51) Bryks, W.; Wette, M.; Velez, N.; Hsu, S.-W.; Tao, A. R. *J. Am. Chem. Soc.* **2014**, *136* (17), 6175−6178.
(52) Ye, M.; Wen, X.; Zhang, N.; Guo, W.; Liu, X.; Lin, C. *J. Mater. Chem. A* **2015**, *3* (18), 9595−9600.
(53) Liu, L.; Zhong, H.; Bai, Z.; Zhang, T.; Fu, W.; Shi, L.; Xie, H.; Deng, L.; Zou, B. *Chem. Mater.* **2013**, *25* (23), 4828−4834.
(54) Van der Stam, W.; Akkerman, Q. A.; Ke, X.; van Huis, M. A.; Bals, S.; de Mello Donega, C. *Chem. Mater.* **2015**, *27* (1), 283−291.
(55) Kumar, P.; Gusain, M.; Nagarajan, R. *Inorg. Chem.* **2011**, *50* (7), 3065−3070.
(56) Wang, M.; Xie, F.; Li, W.; Chen, M.; Zhao, Y. *J. Mater. Chem. A* **2013**, *1* (30), 8616−8621.

DOI: 10.1021/jacs.6b08264
J. Am. Chem. Soc. 2016, 138, 13717−13725